TOLLMIEN-SCHLICHTING WAVE CANCELLATION USING AN OSCILLATING LORENTZ FORCE

Thomas Albrecht, Hans Metzkes and Roger Grundmann
Institute for Aerospace Engineering,
Technische Universität Dresden
D-01062 Dresden, Germany
thomas.albrecht@tu-dresden.de

Gerd Mutschke and Gunter Gerbeth
MHD Department, Institute of Safety Research,
Forschungszentrum Dresden-Rossendorf
P.O. Box 51 01 19, D-01314 Dresden, Germany
g.mutschke@fzd.de

ABSTRACT

Using 2-D and 3-D Direct Numerical Simulations, we present results of Tollmien-Schlichting (TS) wave cancellation in a flat plate boundary layer, where the initial TS wave is supposed to be cancelled out by a secound wave of same amplitude, but 180° phase shifted. Considering low electrically conductive fluids like seawater, an oscillating Lorentz force is used to generate the counter-phased wave. Although the Lorentz force, hence the counter-phased wave, are inhomogeneous in spanwise direction, the remaining wave amplitude is reduced by more than 90% compared to the uncontrolled case.

INTRODUCTION

Given a flat plate boundary layer in a low free stream turbulence environment, the transition from laminar to turbulent flow is initiated by the amplification of small-amplitude, two-dimensional wave-like velocity fluctuations, the so-called Tollmien-Schlichting (TS) waves. Since the turbulent wall friction can exceed the laminar one by more than an order of magnitude, damping of these waves, hence delaying transition, reduces drag. Various methods of actuation have been proposed, where modifying the mean velocity profile by wall suction/blowing is probably the most common one. Although successfully tested even during in-flight experiments, mean velocity profile modification demands a comparably large power input which degrades its efficiency. In contrast, Milling (1981) reported experimental results of wave cancellation by superposition of a counter-phase wave using vibrating wires, requiring only a fraction of control power input. Following this principle, several numerical and experimental works appeared since then, e.g. Liepmann and Nosenchuck (1982) and Kozlov and Levchenko (1987).

If the fluid under consideration is low conductive, such as seawater with an electrical conductivity $\sigma \approx 5\,\mathrm{S/m}$, a Lorentz force acting directly within the fluid is able to control the flow (Albrecht et al., 2006). Driven by an external electric field, almost arbitrary time signals may be generated. An application to wave cancellation is obvious, but, to our knowledge, has not been published before. In the present study, we investigate this numerically.

The paper is organized as follows. In the subsequent section, we give a detailled description of the problem and the computational domain. Lorentz force actuator and the numerical model are introduced in section "Methods". The "Results" section covers extensive parameter variations in both 2-D and 3-D, followed by a summary and discussion.

PROBLEM DESCRIPTION

We consider the transitional flat plate boundary layer flow of a low electrically conducting fluid. The coordinates and flow variables are nondimensionalized using the inflow displacement thickness δ_1 and the free-stream velocity U_∞, respectively, yielding an inflow Reynolds number $\mathrm{Re_{in}} = U_\infty \delta_1/\nu = 585$ with ν denoting the kinematic viscosity. Schematically shown in Fig. 1(a), the computational domain Ω starts downstream of the flat plate's leading edge at $x = -250$, where x, y, z denote streamwise, wall-normal, and spanwise coordinate, respectively. Artificial disturbances are introduced in a region $x_{d0} = -194 \leq x \leq x_{d1} = -138$ near the laminar inflow boundary by means of a body force oscillating at a fixed frequency parameter

$$\mathrm{F}^+ = \frac{2\pi f \nu}{U_\infty^2} \cdot 10^6 = 108 \qquad (1)$$

where f is the frequency. Using the shape function $v_s(x)$ given by Fasel (2002), the non-dimensional, 2-D body force term reads

$$F_d(x, y, t) \quad = \quad A_{2d}\, v_s(x) v_r(y) \cos \frac{\mathrm{Re_{in}}\, \mathrm{F}^+}{10^4} t \qquad (2)$$

with

$$\begin{aligned}
x_{d0} \leq x \leq x_c \quad &: \quad v_s = \tfrac{1}{48}(729\,\xi^5 - 1701\,\xi^4 + 972\,\xi^3) \\
& \qquad \xi = \frac{x - x_{d0}}{x_c - x_{d0}} \\
x_c \leq x \leq x_{d1} \quad &: \quad v_s = -\tfrac{1}{48}(729\,\xi^5 - 1701\,\xi^4 + 972\,\xi^3) \\
& \qquad \xi = \frac{x_{d1} - x}{x_{d1} - x_c} \\
0.01 \leq y \leq 0.39 \quad &: \quad v_r(y) = \tfrac{1}{2}(1 + \cos \pi (y - 0.2)/0.19)
\end{aligned}$$

where $x_c = \frac{1}{2}(x_{d0} + x_{d1})$ is the center of the disturbance strip and $v_r(y)$ restricts the body force to the near-wall region. Since the disturbance input is uniform in z, a two-dimensional TS wave emerges, growing as it propagates downstream. This initial wave is supposed to be canceled out by a counter-phased wave, originating from a Lorentz

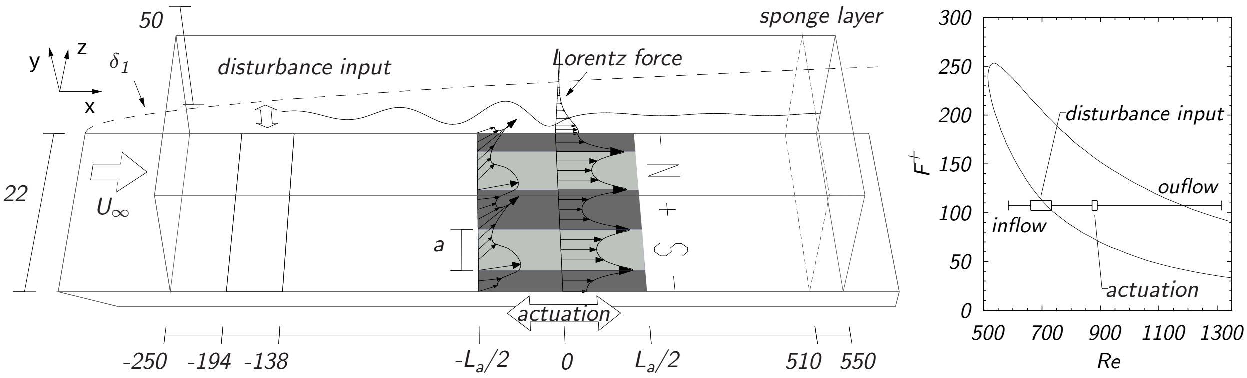

Figure 1: (a) Computational domain Ω, actuator design and resulting Lorentz force. (b) Position relative to neutral stability curve.

force actuator placed at the coordinate system's origin. To prevent unphysical reflections at the outflow boundary $(\boldsymbol{n} \cdot \nabla)\boldsymbol{u} = 0$ at $x = 550$, the remaining wave is artificially damped downstream of $x = 510$ by a sponge layer technique (Guo et al., 1996). Further boundary conditions include a Blasius velocity profile at the inflow, no-slip condition $\boldsymbol{u} = 0$ at the wall, and a second outflow condition at the free-stream boundary $y = 50$. Fig. 1(b) summarizes the main features of the computational domain relative to the neutral stability curve.

Since wave cancelation assumes linear superposition, we will consider cases where either disturbance input or actuator are turned off. To simplify matters, we use the following notation: Type-10 refers to the uncontrolled flow (disturbance input on, actuator off). Type-01 is used to study the wave generated by the actuator only (disturbance input off, actuator on), whereas type-11 denotes the superposition (both disturbance and actuator on), which is the default unless otherwise stated.

METHODS

Lorentz force actuator

A Lorentz force $\boldsymbol{F} = \boldsymbol{j} \times \boldsymbol{B}$ arises from magnetic induction $\boldsymbol{B}$ and electric current density $\boldsymbol{j}$. The latter is described by Ohm's law in moving media $\boldsymbol{j} = \sigma(\boldsymbol{E} + \boldsymbol{u} \times \boldsymbol{B})$, where $\boldsymbol{E}$ and $\boldsymbol{u}$ denote an external, applied electric field and the velocity field, respectively. When assuming $\boldsymbol{B} \approx 1T$ and $u \approx 1m/s$, due to the low electrical conductivity, the induced current density $\sigma(\boldsymbol{u} \times \boldsymbol{B})$ is insufficient to generate a reasonable Lorentz force. Hence, an external electric field $\boldsymbol{E}$ has to be applied. Being much larger than the induced field $\boldsymbol{u} \times \boldsymbol{B}$, the applied one dominates Ohm's law, simplifying the Lorentz force to $\boldsymbol{F} = \sigma(\boldsymbol{E} \times \boldsymbol{B})$. With the magnetic Reynolds number being in the order of 10^{-7}, the low induction approximation holds, where $\boldsymbol{E}$ and $\boldsymbol{B}$ can be computed decoupled from the velocity field during pre-processing as if the fluid was at rest. Finally, both fields are governed by the electro- and magnetostatic equations, thus determined by the actuator's geometry only. We use a periodic array of flush-mounted, streamwise aligned, alternating stripes of permanent magnets and electrodes of changing magnetization orientation and polarity, respectively, each having a constant width a and a length L_a. Solving Laplace's equation for the scalar electric potential $\nabla^2\phi = 0$ by a standard second order finite difference scheme on the computational domain Ω_{EM} shown in Fig. 2 yields the electric field via $\boldsymbol{E} = -\nabla\phi$. Due to the symmetry of the problem, it is sufficient to actually calculate only one fourth of the period length in spanwise direction and half the actuator's length L_a plus a certain far-field region chosen as $L_f = 3a$.

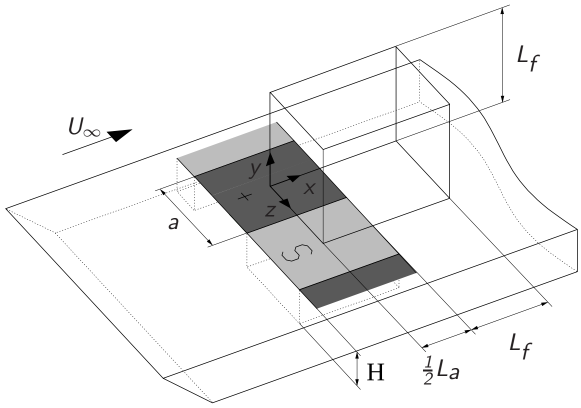

Figure 2: Domain Ω_{EM}
for the computation of the electric and magnetic field.

The electric potential is set to ϕ_0 at the electrode's surface and zero at $z = a$ and the far-field boundaries $x = L_a/2 + L_f$, $y = L_f$, while symmetry conditions were applied at $x = 0, z = 0$ and at the bottom wall not covered by the electrode.

The magnetic induction within Ω_{EM} is obtained from Akoun and Yonnet's analytic solution (Akoun and Yonnet, 1984) for a rectangular surface

$$\begin{pmatrix} B_x \\ B_y \\ B_z \end{pmatrix} = \frac{M_0}{2\pi} \sum_{i=0}^{1} \sum_{j=0}^{1} (-1)^{i+j} \begin{pmatrix} \ln(R - S_i) \\ \arctan \frac{S_i T_j}{R y} \\ \ln(R - T_j) \end{pmatrix} \tag{3}$$

where

$$S_i = z - a - (-1)^i \frac{a}{2} \tag{4}$$

$$T_j = x - (-1)^j \frac{L_a}{2} \tag{5}$$

$$R = \sqrt{S_i^2 + T_j^2 + y^2} \tag{6}$$

Ensuring a balanced number of north and south poles, we included six surfaces to model the periodic array of magnets: Three adjoining to the left (N-S-N) and two to the right (N-S), where the outer ones contributed less than 1% to the magnetic induction in the symmetry plane $z = a$. Using an odd number of surfaces would result in an unphysical change of the sign of B_y beyond a certain distance off the wall. Both

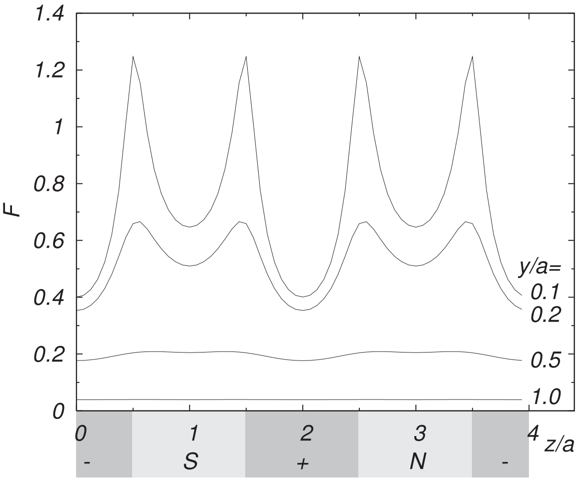

Figure 3: Spanwise distribution of the Lorentz force at the symmetry plane $x = 0$ and different wall-normal positions.

fields were validated using a commercial Maxwell-Solver and experimental data from Weier (2006).

Figure 3 shows the resulting Lorentz force at the symmetry plane $x = 0$, where it is purely streamwise oriented. Being inhomogeneous in spanwise direction z with strong peaks appearing above the electrode's and magnet's edges, the force remains almost entirely streamwise up to a distance a off the actuator's ends. Near the ends, it has significant wall-normal and spanwise components. Its decay in wall-normal direction is approximately exponential and directly related to the actuator's stripe size a, hence, a is also referred to as penetration depth. Similarly, the spanwise inhomogeneity reduces with increasing y. A non-dimensional force amplitude is given by the modified Hartmann number

$$\mathrm{Z} = \frac{j_0 M_0 a^2}{8\pi\rho U_\infty \nu} \tag{7}$$

describing the ratio of Lorentz and viscous forces, where $j_0 = \phi_0\sigma/a$, M_0, and ρ denote the applied current density, the magnetization of the permanent magnets, and the fluid density, respectively. It is related to the interaction parameter N via

$$\mathrm{N} = \frac{Z}{\mathrm{Re_{in}}}\left(\frac{\pi}{a/\delta_1}\right)^2 \tag{8}$$

For 2-D simulations, we calculate the spanwise average of the force, which is approximately described by

$$F = \frac{\pi}{8} j_0 M_0\, \mathrm{e}^{-\pi y/a}\, \mathbf{e_x} \tag{9}$$

when neglecting the non-streamwise components found near the actuator's ends. To produce a counter-phased wave, the force oscillates sinusoidally in time using the TS wave frequency and a phase angle φ relative to the uncontrolled flow's wall shear stress oscillations at $x = 0$. Consequently, we will use the rms-value $\mathrm{Z_{rms}} = \mathrm{Z}/\sqrt{2}$ in the following.

Navier-Stokes solver

The incompressible, non-dimensionalized Navier-Stokes equations

$$\frac{\partial \boldsymbol{u}}{\partial t} + (\boldsymbol{u}\nabla)\boldsymbol{u} = -\nabla p + \frac{1}{\mathrm{Re_{in}}}\nabla^2\boldsymbol{u} + \boldsymbol{F} \tag{10}$$

$$\nabla\cdot\boldsymbol{u} = 0 \tag{11}$$

including the Lorentz force term $\boldsymbol{F}$ are integrated using a well-established spectral element solver by Henderson and Karniadakis (1995) which has already been applied to various MHD problems (Posdziech and Grundmann, 2001; Mutschke et al., 2006; Albrecht et al., 2006). Extending over 800×50 units, the computational domain is decomposed into 85×13 spectral elements of polynomial degree 7. We chose an element size of $\Delta x = 10$ and $0.1 \leq \Delta y \leq 20$, except for the vicinity of the actuator, where Δx is refined to 5. The non-dimensional time step is 0.05, corresponding to 2000 timesteps per TS wave period. For 3-D calculations, the spanwise direction is assumed to be periodic, allowing for a Fourier ansatz for the flow variables, where 32 modes were used.

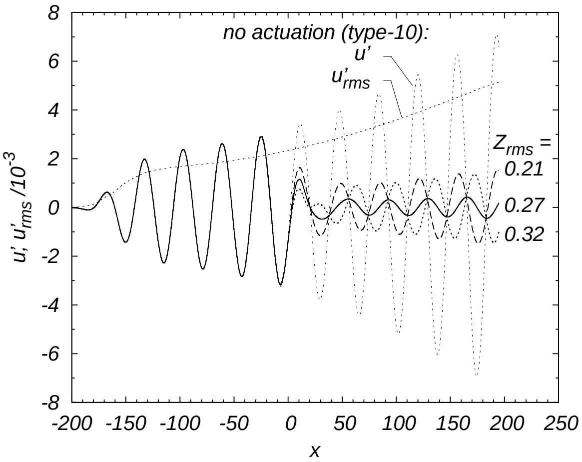

Figure 4: Streamwise velocity fluctuations u' along a line $y = 1$ for $a = 4.5$ and different $\mathrm{Z_{rms}}$. For the uncontrolled case, both u' and its root mean square value u'_{rms} are shown.

RESULTS

2-D simulations

In this section, we will present results obtained from 2-D calculations. Although the "real" Lorentz force is inhomogeneous in z, only 2-D runs using the spanwise averaged force allow for comprehensive parameter variations.

TS waves usually cause a maximum streamwise velocity fluctuation $u'(t)$, defined as the difference between instantaneous velocity $u(t)$ and its time average $\overline{u}$, near $y = 1$. Figure 4 shows u' at $t = 25000$ along a line $y = 1$ throughout the domain for the uncontrolled case and different control force amplitudes. As expected, the uncontrolled fluctuations grow with increasing x. When applying the oscillating Lorentz force, the second wave generated at the actuator reduces the overall fluctuations by superposition. Given a penetration depth a, there is an optimum Lorentz force amplitude yielding maximum TS wave damping. For $a = 4.5$, it has been found to $\mathrm{Z_{rms}} = 0.27$ (solid line). Lower force amplitudes (for example, $\mathrm{Z_{rms}} = 0.21$, dashed line) do not "fully cancel" the wave, while increasing the force amplitude beyond the optimum value causes a phase-shifted wave (for example, $\mathrm{Z_{rms}} = 0.32$, dotted line).

The root mean square value of u', for clarity plotted for the uncontrolled wave only, is appropriate to confidently yield a wave amplitude at every x. Accounting for the boundary layer growth, we finally determine the local TS wave amplitude by finding the maximum root mean square value $\hat{u}'_{rms}$ over the wall-normal direction at given down-

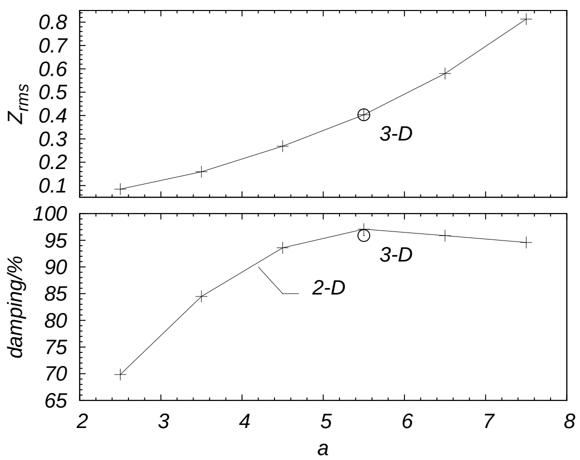

Figure 5: Maximum TS wave damping found for different a, and corresponding force amplitudes Z.

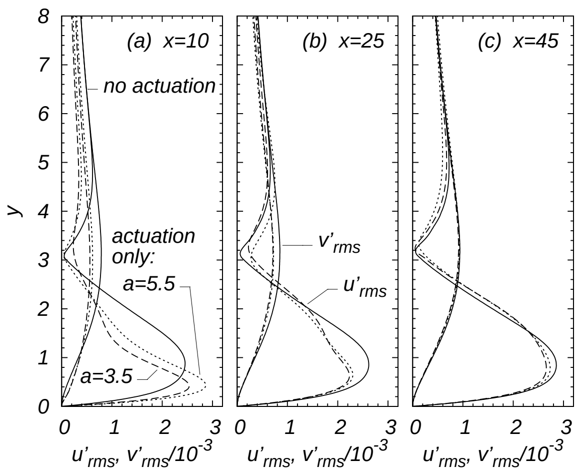

Figure 6: Comparison of TS waves generated by the actuator (type-01) and the disturbance input (type-10) at three downstream locations.

stream position x:

$$\hat{u}'_{rms}(x, z) = \max_{y=0}^{\infty} u'_{rms}(x, y, z) \qquad (12)$$

Measured representatively at $x = 170$, Fig. 5 shows the maximum damping (defined as $1 - \hat{u}'_{rms}/\hat{u}'_{rms,Z=0}$) achieved for different a, as well as the corresponding force amplitudes $\mathrm{Z_{rms}}$. The global maximum damping of 97% is found at $a = 5.5$, $\mathrm{Z_{rms}} = 0.40$, and a phase angle $\varphi = 3.13$ rad $(179.3°)$. At different penetration depths, however, the actuator performs similarly well if $\mathrm{Z_{rms}}$ is adjusted accordingly. This allows for a damping $> 90\%$ within a range $4.5 \leq a \leq 7.5$. Since the *dimensional* stripe size $a \cdot \delta_1$ is usually fixed in an application, this is of practical importance: Varying the free-stream velocity, for example, changes δ_1, and the actuator will be operated at varying *non-dimensional* a.

Since the amplitude reduces only gradually after actuation, there must be an evolution of the canceling wave. Figure 6 shows two waves generated by the actuator only (type-01, dashed/dotted lines) at different a, and the initial TS wave without actuation (type-10, solid line) for reference. Immediately after actuation at $x = 10$, it is clearly shown that the major perturbation energy has been fed into

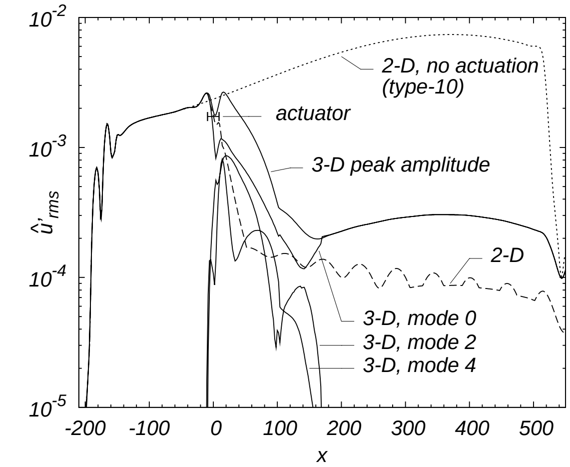

Figure 7: TS wave amplitude vs. x for uncontrolled, 2-D force, and 3-D force case.

the flow below $y = 1.5$. The maximum amplitude is found at $y \approx 0.5$ for both a, which is well below its usual position $y \approx 1$. While the maximum amplitude for the case $a = 5.5$ (dashed line) is clearly larger here, both waves tend to approach each other as well as the "natural" TS wave shape. Optimum cancelation is achieved not until one wave length downstream the actuator's end.

3-D simulations

Now, we will compare results from 3-D calculations using the "real", inhomogeneous Lorentz force distribution with the previous 2-D case. Plotted in Fig. 7, the uncontrolled TS wave (Z = 0, dotted line), being excited in the already unstable region beyond branch I of the neutral stability curve, grows until it reaches branch II at $x = 372$ (local $\mathrm{Re} = 1193$), which is in agreement to nonparallel linear stability theory (LST) results published by Herbert and Bertolotti (1991). Beyond this point, it decreases again, eventually being damped strongly within the sponge region near the outflow boundary. The dashed line represents the global maximum damping found for a 2-D force ($a = 5.5$, $\mathrm{Z_{rms}} = 0.40$, $\varphi = 3.13$ rad): Downstream of the actuation at $-9 \leq x \leq 9$, the amplitude gradually reduces by more than an order of magnitude. For $x > 100$, it oscillates at a level $\hat{u}'_{rms} \approx 10^{-4}$.

When applying an inhomogeneous force (3-D case, solid lines) at the same conditions a, Z, φ, due to the four-peak structure, the TS wave is no longer purely two-dimensional after actuation, but modulated in spanwise direction. To determine its amplitude and two-dimensionality, we extracted the $\hat{u}'_{rms}$-value from the peak plane $z = 0$ (named peak amplitude in the following) and performed a spanwise FFT at these $\hat{u}'_{rms}$ (x,y)-positions, respectively. Following the spanwise distribution of the force, the flow's structure is symmetric in z as well. Therefore, all odd modes are zero, and for clarity, only the first three non-zero modes are shown. All modes except mode 0 being zero would signal a perfectly two-dimensional TS wave.

Similar to 2-D, the mean wave amplitude (mode 0) reduces during actuation, but higher modes initially rise from zero to almost the same level as mode 0, thus indicating a highly three-dimensional TS wave, and actually *increase* the peak amplitude temporary. For $x > 30$, however, all modes decrease, and the higher modes quickly settle down around 10^{-7}. Finally, at $x \approx 180$, the TS wave can be

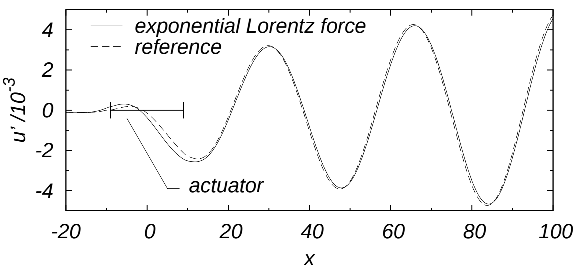

Figure 8: Comparison of instantaneous disturbance velocity u', extracted along a line $y = 1$, generated by the actuator using the exponential force Eq. (9), and the exact, but spanwise averaged force.

considered two-dimensional again, where peak and mean amplitude must coincide. Further downstream, the wave evolves according to LST.

Again measured at $x = 170$, the damping for the 3-D case is included in Figure 5. Compared to the 2-D case it is only slightly degraded.

Is detailled actuator modelling neccessary?

We now want to answer the question whether detailed modeling of the (finite length) actuator is generally necessary. As mentioned above, the Lorentz force decays *approximately* exponential. Implementing the simple analytical expression given in Eq. (9) would be way quicker, however, this neglects the reduced force magnitude and additional non-streamwise force components near the actuator's ends. For this simple model, end effects were included via an exponentially decaying force also in streamwise direction up- and downstream of the actuator. Figure 8 compares the instantaneous disturbation velocity $u' = U - \overline{U}$ extracted from a line $y = 1$ for the exponential and the exact (though 2-D, i. e. spanwise averaged) force using a type-01 setting. We find a small phase shift of 3.5°, and the maximum u' decreases by 1.4%, ($\hat{u}'_{rms}$ decreases by 1.6%). Using the parameters which yield optimum cancelation for the exact force, the TS wave damping in a type-11 simulation reduces to 94%.

SUMMARY AND DISCUSSION

In the present paper we have investigated the effect of an oscillating Lorentz force on the evolution of TS wave. We have shown that, in general, significant amplitude reduction is possible. Depending on the force amplitude $\mathrm{Z_{rms}}$ and penetration depth a, a damping $> 90\%$ is found for a range $4.5 \leq a \leq 7.5$, which is comparable to other published results on wave superposition. Due to the spanwise inhomogeneity of the Lorentz force, the canceling wave, therefore the result of the superposition, is highly three-dimensional. Spanwise modes rise during actuation, however, the flow being secondary stable with fluctuations not exceeding the stability threshold of $\hat{u}'_{rms} \approx 0.01$ at any time, they decay within $\mathcal{O}(100)$ streamwise units. In turn, failing to sufficiently damp the primary amplitude, yet exciting spanwise modes due to the inhomogeneous Lorentz force, certainly triggers transition. However, considering the rather dramatic secondary growth rates, a secondary unstable flow is likely to become turbulent soon, anyway.

Cancelation results from 2-D calculations using a spanwise averaged Lorentz force reasonably correspond to 3-D simulations, allowing for quick investigation of the parameters involved. Applying the analytical but approximate exponential Lorentz force distribution further simplifies modeling at the expense of a 2% accuracy loss.

Finally, the elaborate, but manual adjustment of phase, penetration depth and force amplitude at this quite simple actuator geometry still leaves open questions: What is the optimum distribution of the Lorentz force? Does the efficiency improve if the canceling wave is introduced via a low amplitude, but traveling Lorentz force? What is the effect of different wave forms? In an application, this may easily be achieved using segmented electrodes and an adequate electric current, respectively. However, the increased number of parameters requires an automatic optimization tool, which is currently being implemented.

ACKNOWLEDGMENTS

We are grateful to T. Weier for many fruitful discussions and the group of Prof. G. E. Karniadakis for introducing us into the spectral element code. Computational facilities were provided by ZIH Computing Center, Technische Universität Dresden. Financial support from Deutsche Forschungsgemeinschaft in frame of "SFB 609" is gratefully acknowledged.

REFERENCES

Akoun, G. and Yonnet, J., 1984, "3d analytical calculation of the forces between two cuboidal magnets", *IEEE Transactions on Magnetics*, MAG-20(5) pp. 1962–1964.

Albrecht, T., Grundmann, R., Mutschke, G., and Gerbeth, G., 2006, "On the stability of the boundary layer subject to a wall-parallel Lorentz force", *Phys. Fluids*, Vol. 18, pp. 098103.

Fasel, H. F., 2002, "Numerical investigation of the interaction of the Klebanoff-mode with a TollmienSchlichting wave", *J. Fluid Mech.*, Vol. 450, pp. 1–33.

Guo, Y., Adams, N. A., and Kleiser, L., 1996, "A comparison study of an improved temporal DNS and spatial DNS of compressible boundary layer transition", *AIAA J.*, Vol. 34, pp. 683–690.

Henderson, R. D., and Karniadakis, G. E., 1995, "Unstructured spectral element methods for simulation of turbulent flows", *J. Comput. Phys.*, Vol. 122, pp. 191–217.

Herbert, T., and Bertolotti, F. P., 1991, "Stability analysis of nonparallel boundary layers", *Bull. Amer. Phys. Soc.*, Vol. 32, pp. 2079.

Kozlov, V. V., and Levchenko, V. Y., 1987, "Laminar-turbulent transition control by localized disturbances", In *Turbulence Managment and Relaminarisation*. Springer Verlag, 1987. IUTAM-Symposium, Bangalore, India.

Liepmannm, H. W., and Nosenchuck, D. M., 1982, "Active control of laminar-turbulent transition", *J. Fluid Mech.*, Vol. 118, pp. 201–204.

Milling, R. W., 1981, "Tollmien-Schlichting wave cancellation. *Phys. Fluids*, Vol. 24(5), pp. 979 – 981.

Mutschke, G., Gerbeth, G., Albrecht, T., and Grundmann, R., 2006, "Separation control at hydrofoils using Lorentz forces", *Eur. J. Mech. B/Fluids*, Vol. 25(2), pp. 137–152.

Posdziech, O., and Grundmann, R., 2001, "Electromagnetic control of seawater flow around circular cylinders", *Eur. J. Mech. B/Fluids*, Vol. 20, pp. 255–274.

Weier, T., 2006, "Elektromagnetische Strömungskontrolle mit wandparallelen Lorentzkräften in schwach leitfähigen Fluiden", Technical report, FZ Rossendorf.